Unidirectional emission and reconfigurability of channeled spin waves from a vortex core in a teardrop-shaped nanopatch

D. Osuna Ruiz,[1,2,*] E. L. Martin,[2] A. P. Hibbins,[2] and F. Y. Ogrin[2]
[1]*Department of Applied Physics, University of Salamanca, Salamanca 37008, Spain*
[2]*Department of Physics and Astronomy, University of Exeter, Exeter EX4 4QL, United Kingdom*

(Received 22 April 2021; revised 4 September 2021; accepted 14 September 2021; published 21 September 2021)

We propose the design of a teardrop-shaped magnetic patch as a unidirectional magnetically driven spin wave emitter capable of operating in a wide range of frequencies. We explore its potential through micromagnetic studies in line with vibrational sample magnetometry measurements and ferromagnetic resonance experiments. The proposed system is based on the excitation of a vortex core, acting as a source of spin waves, and a single Bloch domain wall, as a channel for the confinement and propagation of the mode in a sufficiently thick magnetic patch in the single magnetic vortex (SMV) state. The novelty consists in the reconfigurability and simplicity of the system, that is operational without the need of external saturating fields, retaining a *single Bloch domain wall* and *a movable single vortex core*. This allows significant suppression of the wave emission by means of an external bias field, which in turn allows a controllable valvelike effect. Following our proposed strategy for cultivating a single vortex core in the shape, and after a thorough micromagnetic study of the most prominent magnetization dynamics in the patch, we show that the SMV state can be obtained in a thick enough (80 nm) teardrop-shaped patch. Micromagnetic results show the potential of this simple structure as a tunable and unidirectional spin wave emitter. Experimental results also suggest that the required magnetic configuration has been experimentally obtained in the structure, in good agreement with micromagnetic simulations.

DOI: 10.1103/PhysRevB.104.094427

I. INTRODUCTION

A magnetic vortex consists of a flux-closure equilibrium state of circulating in-plane magnetization that surrounds a region of out-of-plane magnetization called the vortex core, with a diameter of only a few tens of nanometers [1]. Vortex states in ferromagnetic thin films can support a rich spectrum of spin waves in addition to minimizing the in-plane stray field; this makes them promising candidates to exploit propagating spin waves as information carriers in micrometer and submicrometer scale magnonic circuits [2–7]. As has been shown in previous works, inhomogeneities such as vortex cores have been widely studied as coherent spin wave emitters [6–10]. These emitted waves can also be channeled along domain walls at low enough frequencies [9]. Once the spin wave is emitted, an adequate control of its propagation is key for the developing of circuits that conducts the spin wave through magnonic channels. Local excitation of spin waves and its spatial confinement has been widely studied in terms of local ferromagnetic resonances due to an inhomogeneous demagnetizing field [5,11]. More specifically, confinement along the edges [12,13], in domain walls and by domain wall natural fluctuation modes (or so-called Winter magnons [14]), or in other anisotropic " spin textures" [9,15]. Domain walls act as natural channels for spin waves [16,17], while Winter magnons are very useful for efficient spin wave channeling in a wide range of frequencies. All of the above results in a new degree of control for spin waves that has led to a new subfield of magnetism, which has been termed 'topological magnonics' [15].

Regarding control of spin wave propagation, spatially localizing spin wave energy or confinement of the wave is a key point. Therefore, the interest is on spin waves emission along a single direction of propagation, thus showing a maximum confinement and directivity and ideally leading to a point-to-point spin wave transmission. Previous studies have shown the possibility of steering spin waves by using external biasing fields in Y-shaped structures which, while saturated, allow propagation along different arms of the structure depending on magnetization orientation [18]. This obviously requires external biasing and attached secondary structures to provide such a localized field, which makes designs/devices rather suboptimal.

In this work we explore a simple way of achieving unidirectional, channeled propagation, based on a very simple configuration, consisting of *a single vortex core* as the source and a stabilized *single Bloch domain wall* as the channel, pinned at the shape's single corner. The required contour of the patch resembles a " teardrop" or "raindrop" shape. This is a simpler configuration than other implementations found in literature that typically show at least two domain walls, mostly based on flux closure Landau patterns in square elements [19], ellipses [9], combinations of disks and squares [20], or more complex nanodisk-film composite bilayer structures [21].

In the absence of external biasing fields, the required single core and wall are obtained and stabilized by the single influence of shape anisotropy, so no external fields are required

*d.osuna-ruiz2@exeter.ac.uk

to retain such magnetic configuration. In addition to this, due to the asymmetry of the shape, the influence of a biasing field leads to a different behavior of the confined modes. The teardrop structure could be regarded as the building block of switchable, simple and compact spin wave devices, as will be shown in the next sections. The anisotropic behavior of the shape will be analytically, numerically, and experimentally proven using vibrational sample magnetometry (VSM) and vector network analyzer–ferromagnetic resonance (VNA-FMR) measurements.

II. MATERIALS AND METHODS

To obtain insight into the magnetization dynamics in this shape, we performed a set of micromagnetic simulations using Mumax3 [22]. We simulated a teardrop shape with typical material parameters of Permalloy at room temperature, with saturation magnetization $M_s = 7.6 \times 10^5$ A m^{-1}, exchange constant $A_{ex} = 1.2 \times 10^{-11}$ J m^{-1}, Curie temperature from a weighted average of iron and nickel $T_C = 710$ K, and Gilbert damping constant $\alpha = 0.008$. In addition to these parameters, the single circular disk was simulated in an orthorhombic grid [22]. A teardrop-shaped disk was simulated in accordance with the dimensions of the measured shape, diameter d of 1500 nm, thickness t of 80 nm, and vertex angle of 60°. The grid was discretized in the x, y, z space into 512 ×512 ×16 cells. The cell size along x and y was set to be 3.9 nm, while the cell size along z was set to be 4 nm. The cell size along three dimensions was always kept smaller than the exchange length of Permalloy (5.3 nm) [23]. The number of cells along x and y were chosen to be powers of 2^8 for computational efficiency. The edges of the disk were smoothed to reduce staircase effects from orthorhombic cells. The smoothed edge volume is found by averaging p^3 samples per cell, where p is the parameter input to the function. Since the geometry is a curved shape, the " SmoothEdges" function was set to its maximum value ($p = 8$) [22].

In the first stage of the micromagnetic simulations, the stable equilibrium magnetization state was simulated. A vortex state with counterclockwise circulation (circulation index 1) and core polarization towards the substrate (polarization index −1) was manually set as the initial state and then allowed to relax in a simulation with a high damping parameter ($\alpha = 1$). This particular configuration of core polarization and circulation reproduced the experimental findings as discussed in Sec. IV. The magnetization continued to relax until the maximum change in induction reached 10^{-7} T, indicating convergence to the equilibrium vortex state of magnetization. The maximum change in induction was defined as the " MaxTorque" parameter in Mumax3, which describes the maximum torque/γ over all cells, where γ is the gyromagnetic ratio of the material. The enhanced damping parameter allowed the model to relax to the equilibrium state efficiently. Once the required equilibrium state was obtained, the spin configuration of the disk was recorded and then used as the initial state for simulations with a pulsed magnetic field excitation. To achieve a uniform excitation across a desired frequency range in the dispersion diagram, an (unnormalized) sinc-shaped magnetic pulse has been used, defined as $[B_1(t)]$:

$$B_1(t) = A_1 \mathrm{sinc}[2\pi f_c(t - t_d)] = A_1 \frac{\sin[2\pi f_c(t - t_d)]}{2\pi f_c(t - t_d)}, \quad (1)$$

where f_c is the microwave excitation cut-off frequency, which was set to 30 GHz, and A_1 is the pulse amplitude, set to 10 mT. Using this activation, each mode is equivalently fed with an AC (rf) magnetic field of 0.3 mT in amplitude. This field is small enough to remain in the linear regime of activation and to avoid any static changes in the magnetic domain structure of the samples. t is the time variable. The delay time $t_d = 5$ ns provides a reasonable offset to the peak of the pulse, allowing a gradual increase of the amplitude from the beginning of the simulation. When analyzing time evolution of the magnetic signal, we apply a continuous wave excitation with a magnetic field B_2 at a specific frequency f_0:

$$B_2(t) = A_2 \sin[2\pi f_0 t)], \quad (2)$$

where A_2 is the pulse amplitude. Similar to the sinc pulse, each mode is excited with a relatively small oscillating field. Equivalently to the previous case, A_2 is chosen to be 0.3 mT to obtain a good magnetic contrast in the time domain. A sampling period of $T_s = 25$ ps was used, recording up to 1024 simulated snapshots in space and time, only after the steady state is reached. With these parameters, the Nyquist criterion [24] was satisfied for the whole range of frequencies used in our study.

In our measurements we used a set of samples fabricated using standard electron beam lithography techniques [25,26]. To enhance the rf and magnetic response, the elements were grouped in square lattices with the separation equal to the size of the element. We tested arrays of thick ($t = 80$ nm) teardrop shapes with 1.5 μm of diameter (of the circumscribed circle) and a 60° vertex. Given the magnitude of the oscillating field (less than 1 mT) and since the effective separation between vortex cores in the sample array is approximately 3000 nm (equal to the interdot distance plus the diameter of the disk), we consider interelement coupling due to dipolar interactions to be negligible when compared to the Oersted field [27,28]. Experimental hysteresis results were obtained by vibrational sample magnetometry and dynamical results where obtained by measuring the transmission spectra of a sample in a coplanar waveguide geometry using a VNA-FMR setup applying an in-plane excitation [29,30]. The spectra were visualized through the real part of magnetic susceptibility (χ'). Since the arrays of samples are placed on top of a coplanar waveguide (CPW), the pumping magnetic field provided by the CPW can be applied parallel or perpendicular to the major axis of the sample (i.e., parallel or perpendicular to the domain wall). The sample is placed on the short path of a U-shaped CPW, and so, perpendicular " pumping" with respect to the biasing field is applied ($H_{\mathrm{bias}} \perp h_{\mathrm{rf}}$) to efficiently excite spin waves in dynamic vortex regimes near nucleation or smaller than vortex-annihilating fields [30]. The experiments were carried out as sweeps in the biasing field, in the range of 0–70 mT in steps of 2 mT. This range was sufficient to cover the vortex structure regime in the elements as well as near saturation regimes. Each spectrum was reduced by subtracting the signal produced at a highest field, and then averaged over ten measurements. This aided in removing the larger background

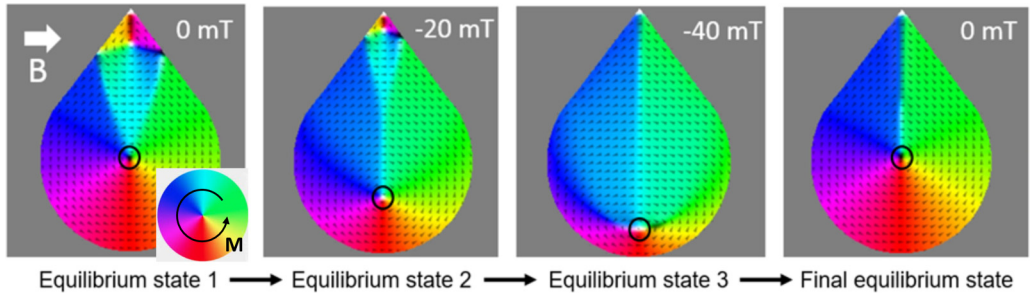

FIG. 1. Field sequence (from left to right) for the magnetic configuration in the simulated teardrop-shaped element. Color wheel indicates the in-plane magnetization orientation. White arrow and values are the applied external biasing field before leaving the shape to relax in order to get a single vortex core and single domain wall, pinned at the sharp corner.

signal related to the transmission line noise, and therefore allowed us to increase the contrast of the magnetic response, which is normally much smaller than other electromagnetic components.

III. MAGNETOSTATIC STUDY OF THE TEARDROP PATCH

In this section, we explore the magnetostatic response of the teardrop shape through micromagnetic simulations. This section is divided into two parts: (a) the steps to achieve the necessary equilibrium state with a single domain wall and (c) the effects of external biasing fields on the domain wall position and the simulated and experimental hysteresis curves for the two different bias field directions. In the following sections, we use the word(s) " saturation" or "saturation fields" to refer to vortex/domain wall annihilating fields, and not necessarily to biasing fields of the same magnitude as the saturation magnetization of the material.

A. Routine to induce the single magnetic vortex state in the patch

Figure 1 shows the equilibrium state of a 1500-nm-wide (diameter of the circumscribed circle), 2000-nm-long from the base to the vertex, and 80-nm-thick patch in the shape of a teardrop, with a corner angle of 60°, after applying an in-plane vortex-annihilating, near saturation field along the x direction and then being removed for relaxation of magnetization. Note that, from numerical results, the obtained equilibrium state is not the single vortex connected by a domain wall to the vertex of the shape. Instead, a second vortex core is nucleated close to the vertex. A "double magnetic vortex? (DMV) stable state has been observed in thin enough circular patches [31,32]. From Ref. [31], this stable state should not be expected in circular patches as thick (80 nm) as the presented teardrop patch. However, introducing the sharp corner allows us to obtain an asymmetric DMV metastable state for thicker samples by breaking the top-bottom symmetry of the shape. This way, the DMV as equilibrium state seems to be allowed because it partially recovers the inversion (or odd) symmetry about a central point in the cyan domain (see Fig. 1), while minimizing stray field. A similar behavior was observed in elliptical shapes when biasing fields along their short axes were applied [33].

However, to allow the Winter's magnon to reach the top vertex without impediments, a single vortex state and a single domain wall connecting with the vertex are required. To obtain a centered single magnetic vortex state (SMV) from a DMV state as the initial equilibrium state, the topmost vortex core must be " expelled" by self-annihilation by applying a strong enough, vortex annihilating, biasing field transversal to the wall, without saturating the sample. To this end, the process proposed here is as follows: As a first step in numerical simulations, a biasing field of −40 mT is applied. The bias field is chosen so it is strong enough to expel the top vortex core and less than vortex annihilation fields to retain the centered vortex core. After the vortex core at the corner is self-annihilated in the new equilibrium state (equilibrium state 3 in Fig. 1), the external field is removed, and the shape reaches again a new relaxed state. The total energy of the shape was recorded after each step of the field routine as well as after the relaxation process in simulations. The convergence to the values of 1.0224×10^{-15} J for the DMV state and 9.4736×10^{-16} J for the SMV state reveal that both states are equilibrium states of the teardrop shape, and that the SMV is of lower energy.

This process is performed as a first step always and the obtained final equilibrium state is saved as the initial magnetic configuration, before any dynamic excitation in simulations. The same routine is performed in experiments before taking measurements.

B. Effect of an external bias field on the single domain wall

Since external biasing fields will displace the vortex core from its former central position in the patch in the SMV state, the domain wall is expected to correspondingly elongate or shorten before the core reaches the new equilibrium position [see Fig. 2(a) for a biasing field of 10 mT perpendicular to the wall]. The core displacement is ultimately caused by the additional dipolar energy engendered by the bias field in the shape. In turn, the domain wall concurrently elongates/shortens as a result of an increase/reduction of the domains aligned with such demagnetizing field. For a parallel bias in the $+y$ $(-y)$ direction, the approach of the wall to the straight edge is energetically expensive, as the orientation of the magnetization in the blue (green) domain is increasingly perpendicular to the edge. This will cause the former domain wall (DW) to split

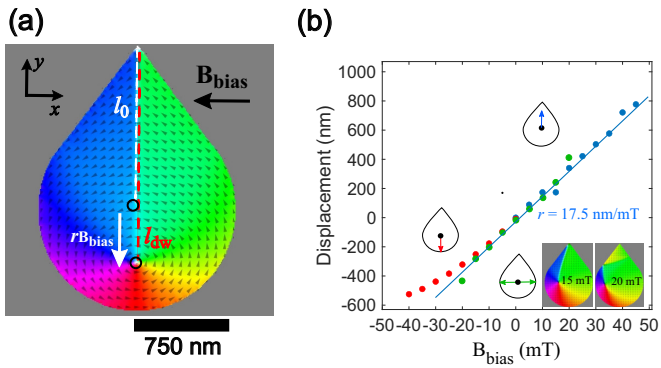

FIG. 2. (a) Domain wall length (red dashed line) when a biasing field is applied perpendicular to the wall. White arrow shows the core displacement as a result of a biasing field of 20 mT in the $-x$ direction (black arrow) and black circles show the initial and final positions of the core after relaxation. Color scale is the angle of in-plane magnetization. White dashed line shows the domain wall length in the equilibrium state (l_0). (b) Vortex core displacement as a function of the biasing field for three different directions, towards the vertex (blue dots), towards the curved edge (red dots), and towards the sides before the domain wall splits (green dots). Insets show a schematic of the core displacement (color arrows) and the obtained values for the slope (ratio r) from a linear fitting to the former dataset. As in (a), the bottom-right insets are the magnetic configurations in the teardrop shape for 15 and 20 mT bias in the $+y$ direction, showing the domain wall splitting.

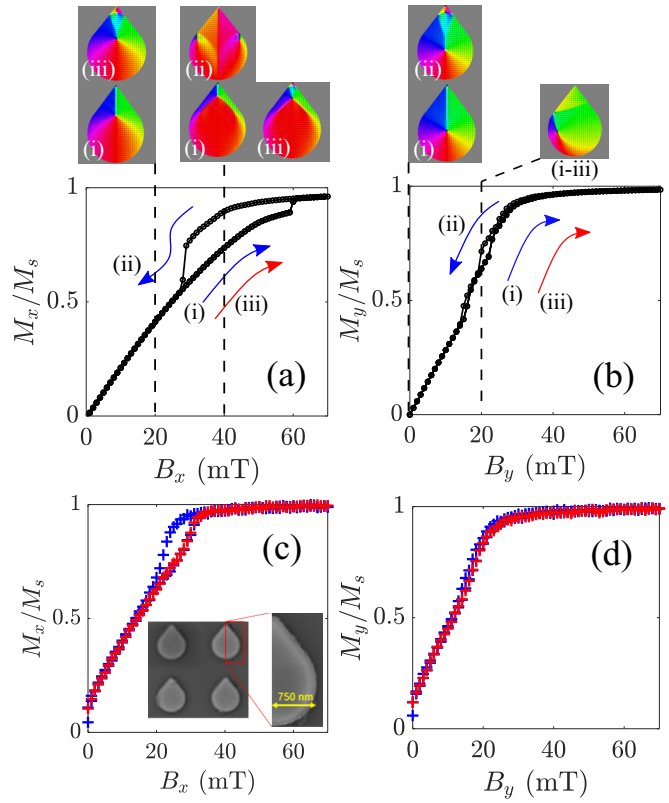

FIG. 3. Simulations of a hysteresis half-loop for the teardrop shape starting from a SMV state with a biasing field applied perpendicular (a) and parallel (b) to the single domain wall and experimental measurements (c) and (d), respectively. Top insets show the magnetic configurations at the indicated biasing fields (0, 20, and 40 mT) for each hysteresis path (blue or red arrows) and sweeps of the bias field [(i)–(iii)] from the model in simulations. Inset in (c) shows a SEM (Scanning Electron Microscopy) picture of four shapes in the sample and a magnification of one half and corner of a single teardrop in the array.

and the vortex core to merge with one half of the split DW at the bottom half of the shape.

From micromagnetic simulations, Fig. 2(b) shows the vortex core equilibrium position displacement as a function of the biasing field for the most significant directions: towards the vertex, towards the curved edge, and towards the sides (blue, red, and green symbols, respectively). An approximately linear behavior with the magnitude of the bias field (fitting blue solid line) is obtained. These micromagnetic results agree well with previous work such as that of Ref. [34], in which the ratio (r) is found to be constant [yielding a more linear displacement; see blue dots in Fig. 2(b)] when the core approaches a vertex in a triangular shape rather than the edge of a circular disk. On the contrary, the displacement is nonlinear close to the circular edge due to the inhomogeneous demagnetizing field in the shape [see red and green dots at high bias in Fig. 2(b), before domain wall splitting]. Insets are schematics showing the vortex core positions at particular bias and the splitting of the DW for a parallel biasing. The teardrop shape can be regarded as a combination of both scenarios, a combination of a circular disk (bottom half) and a triangular patch (upper half).

In a teardrop shape, displacing the vortex core towards (or away from) the vertex by applying a biasing external field (B_{bias}) perpendicular to the wall, implies a shortening (or elongation) of the domain wall length in initial equilibrium (l_0). We simply model this new domain wall length as $l_{\text{dw}} = l_0 + rB_{\text{bias}}$, where r is the vortex displacement to bias field ratio, extracted from a linear fit to micromagnetic experiments (see Fig. 2). Similarly, if the field is applied parallel to the wall, the new length of the domain wall can be expressed as $l_{\text{dw}} = \sqrt{l_0^2 + (rB_{\text{bias}})^2}$. The latter holds until additional vortex cores nucleate near the edge and the former single wall " splits," giving rise to a new triangular domain in the patch, for about 17 mT bias in the $+y$ direction [see insets in Fig. 2(b)].

Figures 3(a) and 3(b) show the simulated hysteresis loops for a 2×2 array of teardrop shapes in the SMV as initial state when the biasing field is applied perpendicular (a) and parallel (b) to the domain wall. Insets only show one teardrop shape from the array as an example. Despite the fact that we observe some teardrops to fall naturally into the DMV or SMV states, we obtained identical hysteresis loops to those from a single teardrop after the SMV state was induced, as shown in Fig. 1. The model was saturated to 70 mT and then allowed to relax after removing the bias field. A sequence of sweeps from 0 mT bias to saturation (70 mT), back to 0 mT and back to 70 mT again are indicated by the (i), (ii), and (iii) indices, respectively. From the results generated from the simulations, there are several key observations. Firstly, the DMV and the SMV can appear naturally after relaxation of the saturated sample (descending hysteresis curve down to 0 mT), implying that both are equilibrium states of the patch. Secondly, both states, SMV and DMV, appear indistinguishable from magnetostatic

data (hysteresis curves below ∼30 mT practically overlap) except that they show very small and different remanence in the x direction. This was calculated from simulations to be around -6261.7 A m^{-1} for the SMV state and -4639.14 A m^{-1} for the DMV state (8.4% and 5.9% of magnetization saturation, respectively). These numbers are obtained for the parameter values shown in Sec. II. Thus, nucleation of a second vortex in the DMV state reduces magnetic remanence by approximately 26%, compared to the SMV state. Thirdly, in a perpendicular biasing scheme, the "returning path" [blue solid arrow for sweep (ii) in Fig. 3(a)] from 70 mT shows the formation of a different configuration similar to a double C or " buckling" state, where two opposite " quasi vortex cores" or Bloch domain walls at the shape boundary are formed [35]. This allows the shape to retain high in-plane magnetization in the x direction and a left-right symmetry [see inset at 40 mT in Fig. 3(a) for sweep (ii)] with further reduction. In-plane magnetization is abruptly reduced around 30 mT, indicating a more abrupt nucleation in the sample than for the parallel biasing. This nucleation field indicates the beginning of vortex state configurations in the shape, leading to the SMV or the DMV equilibrium state as confirmed by micromagnetic simulations [see insets in Fig. 3(b) at 0 mT].

In a parallel biasing [see Fig. 3(b)], the loss of smoothness in the simulated hysteresis curve (from approximately 20 mT of bias) can relate to the nucleation of secondary vortex cores at the edges, with the consequent " splitting" of the single domain wall [see insets in Fig. 3(b)]. A low hysteretic behavior, due to the " left-right" symmetry in the shape, can be observed as well as Barkhausen jumps before reaching near saturation regimes. The jumps can be associated with the magnetic inhomogeneities formed due to the Bloch domain walls pinning and unpinning at the shape boundary during the core shift [see inset at 20 mT in Fig. 3(b)].

Figure 3(c) shows experimental results that confirm the hysteretic behavior of the teardrop shape for the perpendicular biasing scheme. Blue and red crosses correspond to the ascendant or descendent paths (blue and red arrows) from the simulation sweeps. Both saturation and state changes seem to be achieved with lower fields than in the simulated model. This could be explained with smaller samples in reality, which would allow the vortex core to reach the shape contour earlier. Edge defects at the sharp corner could significantly contribute to this, since it is a very delicate feature to resolve accurately, as can be seen in the inset in Fig. 3(c). Also, not all shapes in the array may have the same circulation (counterclockwise in simulations for all shapes), which could contribute with a small but different component to the overall magnetostatic response and reach saturation with smaller fields. Figure 3(d) shows experimental results for the parallel biasing scheme, with very good agreement with simulations, even reflecting the simulated roughness in the hysteresis return path [see blue arrow for sweep (ii)]. In general, experimental results from Figs. 3(c) and 3(d) qualitatively and quantitatively agree well with simulation results shown in Figs. 3(a) and 3(b).

IV. MAGNETOACTUATED DOMAIN WALL RESONANCE

As a starting point, we investigate how a confined mode in the formed domain wall (or Winter's magnons) propagates

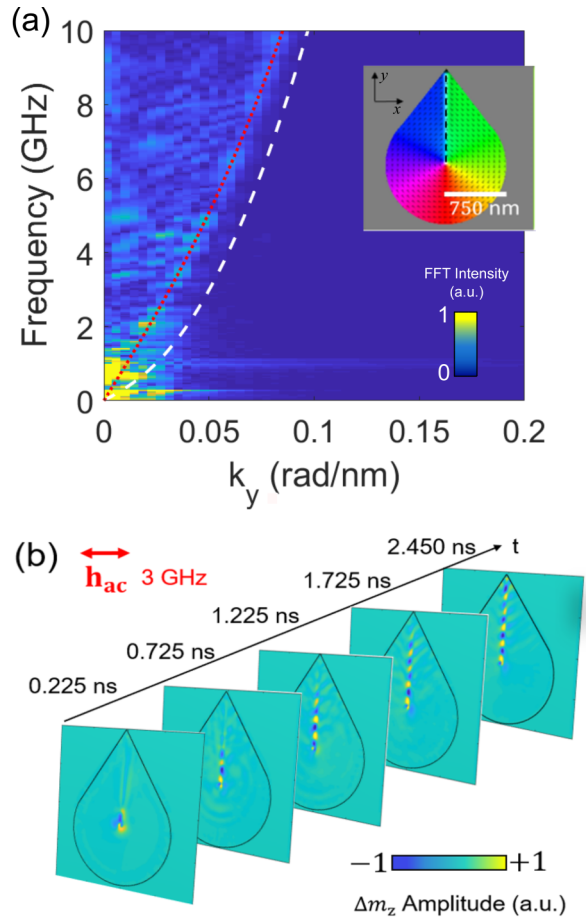

FIG. 4. (a) Simulated dispersion relation along the domain wall in the y direction (black dashed line in inset) in a teardrop shape of given dimensions (color plot). The dispersion relations from a Winter's magnon along a 180° Bloch wall (white dashed curve) and accounting for a transversal demagnetizing field of 0.06 T (red dotted curve) from Ref. [36] are plotted for comparison to the micromagnetic results from the 60° Bloch-Néel wall in the patch. (b) Simulated time sequence of the dynamical out-of-plane magnetization for the middle layer of the micromagnetic model after applying an in-plane oscillating field of 3 GHz in the x direction.

in this shaped element by micromagnetic simulations. Winter's magnons are gapless modes that show the largest wave numbers in a Bloch domain wall with no magnetic anisotropy perpendicular to the wall [36]. In the teardrop shape, the 60° corner introduces a nonzero perpendicular anisotropy, which effectively reduces the confined spin wave wave number. This anisotropy can be modeled as the effect from a transversal dipolar field to the confined wave in the domain wall [36]. In terms of ferromagnetic resonance, it is more appropriate to speak of the " effective field." Although, we must emphasize that we do not distinguish between this and the demagnetization field in our discussion, since the latter is typically its dominant component. In fact, data extracted from the magnitude of the effective field, instead of the demagnetizing field, yield qualitatively equivalent results.

Figure 4(a) shows the simulated (color plot) dispersion relation for the Winter's magnons along the path connecting the vortex core with the vertex in the teardrop shape. In

comparison with the analytical dispersion relation from [36] for Winter's magnons in a 180° Bloch wall (white dashed curve), the simulated dispersion in our shaped patch gives rise to longer wavelength spin waves for the same excitation frequency. This behavior is reminiscent of a Néel-type wall [36], suggesting that the wall profile shows a mixture of Néel and Bloch wall profiles as shown in other works [37–39], due to the corner angle. When an additional anisotropy term (due to the 60° sharp corner) is considered, the dispersion relation of a Winter's magnon in a Bloch wall can be expressed as $f_k^B = \sqrt{f_k(f_k + f_\perp)}$ (see Ref. [36]) where f_k is the dispersion relation for Winter's magnons in a 180° Bloch wall (the quadratic exchange part) and $f_\perp = 2\gamma K_d/M_S$ models an anisotropy transverse to the wall. The anisotropy term K_d can be expressed in terms of a dipolar field (H_d) transversal to the wall, $K_d = \mu_0 M_S H_d/2$. Figure 4(a) shows the fit for this equation (red curve) to results from simulations, yielding an optimal value for H_d of approximately 0.06 T. Note that in reality, this magnitude is spatial dependent in the extension of the length of the wall in the y direction. This is due to the "top-bottom" asymmetry of the shape, which may explain the more noticeable mismatches for longer wavelengths ($k <$ 0.025 rad/nm) between simulations (brightest yellow areas in the color plot) and the fitting curve.

According to the simulations, the mode is of shorter wavelength than in a 180° Bloch wall, as long as it is stable in a range of bias fields and in a wide range of frequencies. Figure 4(b) shows that for an in-plane oscillating field with frequency 3 GHz applied to the whole shape along the x direction, a strongly confined mode propagates in the domain wall from the core towards the sharp corner. The animation is included in the Supplemental movies, as well as the mode profiles for other excitation frequencies (in the range of 1–10 GHz) for which Winter's magnons were also excited [40]. Results correspond to the simulation in the central layer of the model, 40 nm deep from the top surface. Since the excitation field is applied perpendicular to the wall, the origin of the confined mode can be regarded as a stringlike resonance or flexural mode of the wall—or Winter's magnon—where the vortex core is actively excited as it serves as the source of the one-dimensional (1D) spin wave [9]. In a parallel biasing configuration, and while the domain wall is not split, Winter's magnons are still expected to propagate along the domain wall [17]. However, their amplitude might be slightly attenuated, as the parallel bias partially increases the internal magnetic field in the wall, as in (but not as much as in) the perpendicular and negative" biasing scheme. Similar propagation behavior is expected in the DMV state, but it lacks unidirectionality due to interferences between different modes. This is expected since the DMV presents two DWs diverging from the core region, and pinned walls connected to the top vortex will emit additional spin waves as revealed by additional micromagnetic simulations (see Sec. III in the Supplemental Material [40]). The SMV state stands out as the only equilibrium state in which unidirectionality and tunability are achieved.

Figure 5(a) shows simulated wave profiles in the teardrop shape in the SMV state, for several biasing fields and an excitation AC field (3 GHz), applied transverse to the wall, after 2.45 ns from its activation. Each of the corresponding animations are included in the Supplemental movies document

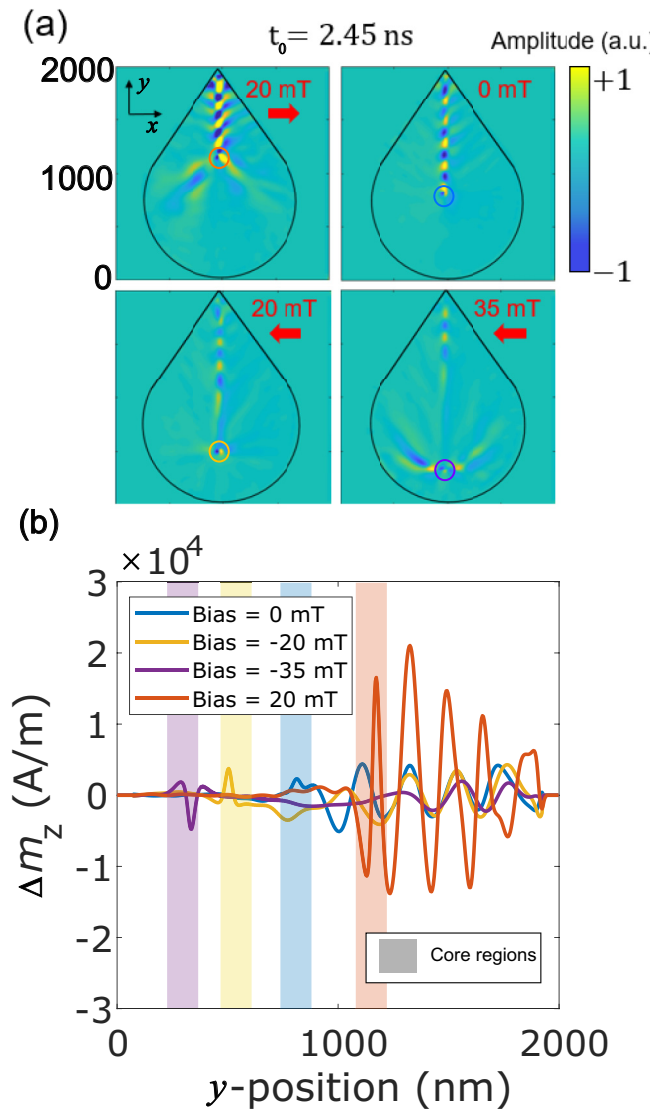

FIG. 5. Simulated spin wave profiles (amplitude) for the dynamic out-of-plane component of magnetization Δm_z for different biasing fields for a given time $t_0 = 2.45$ ns after the excitation field is activated (a). Spatial dimensions are given in nanometers and the color circles show the position of the vortex core. Spin wave profiles and their amplitudes along the formed domain wall (in the y direction) are also shown (b). Shaded areas show the extension of the vortex core region for each bias.

[40]. Depending on the biasing field intensity and orientation, one can see how the amplitude of the spin wave can be significantly enhanced or reduced in the domain wall. The emitted spin wave from the core can more easily propagate in the domain wall (l_{dw}) as far as 1.4 times longer (−20 mT) than without bias (0 mT). This is without a significant reduction in amplitude at its destination at the vertex of the shape [see blue and yellow curves in Fig. 2(b)]. We performed more analytical, micromagnetic, and experimental studies on the resonance conditions of the Winter's modes in the teardrop shape, which can be found in the Supplemental Material [40].

The spin wave reflection or transmissibility properties result from the change of the DW normal modes [41], which

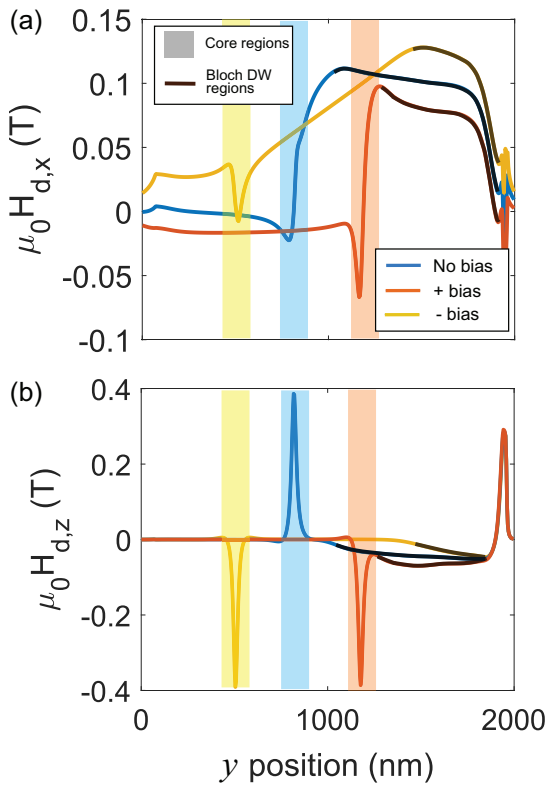

FIG. 6. Simulated in-plane component of demagnetizing field transversal to the wall (a) and the out-of-plane component (b) in absence of biasing (blue curve) and with +20 mT bias (orange curve) and −20 mT bias (yellow curve). Shaded areas show the extension of the vortex core region for each bias. The darker parts of the color curves show the spatial regime (or extension in y) of the Bloch domain wall, and the corresponding values of the demagnetizing field there.

are linked to the spatial inhomogeneity of the effective field in the DW. In our scenario, other observed effects also account for these changes: (1) The additional variation of the internal field due to the biasing fields (as addressed in [36]) and (2) the splitting of the DW into Néel and Bloch types due to the displacement of the vortex core. The latter situation is considered as a 1D analogy to the scenario explored in Ref. [42], where the transmissibility of a two-dimensional spin wave through a DW is generally enhanced if the wall type is a Néel type or a wide enough DW. The work from Wang *et al.* [41] explored the transmissibility across domain walls. Transmissibility is enhanced where there is less variation across the wall of the component of the internal field perpendicular to the sample plane. In the next paragraphs, we explore these ideas applied to our teardrop shape by studying the in-plane and out-of-plane components of the spatially dependent demagnetizing field in the wall for different external biasing fields.

Figure 6 (top panel) shows the in-plane component of the demagnetizing field transverse to the wall (in the x direction) at its center width, for no biasing field (blue curve), and biasing fields of −20 mT (yellow curve) and 20 mT (orange curve). Also, for the out-of-plane component of the demagnetizing field, in the z direction (see bottom panel in Fig. 6). The extension width of the core region is shaded in the respective color of the bias. From numerical results, the core width is assumed to be about 100 nm. The beginning of a Bloch-type wall can be easily identified where the out-of-plane component of the demagnetizing field ($H_{d,z}$) deviates from 0 T (see bottom panel in Fig. 6, dark color sections of the curves). At positive biasing fields, one can see how the separation between the core region, i.e., source of the spin wave, and the Bloch domain wall region is minimal (see positions at the right edge of shaded areas and the beginning of the dark section of the curves in Fig. 6). This implies similar values of the demagnetizing field $H_{d,x}$ and therefore, a " continuous medium" for the spin wave transmission. A less favorable scenario for spin wave transmission is found for negative biasing fields as the difference in $H_{d,x}$ between both positions is greater (i.e., larger separation between the solid dark yellow curve and the yellow shaded area).

At this point, it is worth commenting on these results from the perspective of the local ferromagnetic resonances in the wall, as they are intimately related to the local effective fields in regions of magnetic inhomogeneity [5]. When the local demagnetizing fields do not differ significantly between neighboring regions, the local FMRs are also alike [5,13] and the spin wave is better transmitted along that path. In the case of our proposed shape, the path is the DW instead of the edges as in [5,13]. It is worth noting that the thickness of our sample (80 nm) is key for channeling to occur, since a Bloch DW develops (showing out-of-plane components in its majority). In thinner elements, the formation of Néel DWs (in-plane components in its majority) instead of a Bloch (or a mixed Bloch-Néel DW), can suppress the " continuity" of the magnonic landscape in the DW, between the core and the corner (with out-of-plane magnetization), due to a greater variation along the DW of the effective field (as explained before).

Figure 6 (bottom) also shows that the vortex core can flip polarity when a biasing field is applied. m_z changes from negative to positive, and the opposite for the out-of-plane demagnetizing field $\mu_0 H_{d,z}$, from 0.4 T to −0.4 T. In contrast, the initial positive polarity of the Bloch wall may remain the same (+1). This implies a gradient in orientation of the out-of-plane component of magnetization between both regions and therefore, of the demagnetizing field as well. We believe this relates to the observed different amplitudes of the confined spin wave at different biasing fields, due to the reflections of a spatially dynamic stray field, as addressed in Ref. [42]. This hypothesis may also explain why the spin wave amplitude increases when the wall is shortened (i.e., at positive biasing fields): First, note that there is smaller gradient along the direction connecting the core (polarity = +1) with the wall (polarity = +1) as they show the same polarity (see orange curve in the bottom figure in Fig. 6), than in the absence of biasing fields (blue curve). When a negative bias field is applied (yellow curve in Fig. 6), and even though the core polarity is the same as that of the wall (+1), the out-of-plane component of magnetization ($\mu_0 H_{d,z}$) between the core and approximately 1500 nm in the Néel wall component, is practically zero. This inhibits the propagation of a large amplitude spin wave in that region, since it introduces a more prominent gradient in the orientation of the out-of-plane component of

magnetization m_z, in the y direction (from $+1$ to 0 in the Néel wall region, and back to $+1$ again). In this case, the polarity of the vortex core (either $+1$ or -1) loses relevance for the wave to propagate efficiently, since it would have to cross through a Néel wall region of "zero polarity" regardless.

For negative bias fields and for no bias, values of the in-plane demagnetizing field ($H_{d,x}$) in the wall region are greater than the out-of-plane component ($H_{d,z}$), suggesting that the Néel component in the wall is more prominent in those scenarios. For positive bias, the out-of-plane component of the demagnetizing field ($H_{d,z}$) increases in magnitude as the in-plane component is reduced. For a bias of 20 mT (orange curves in Fig. 6), the proportion between $\mu_0 H_{d,x}$ and $\mu_0 H_{d,z}$ is similar, about 0.075 T about the central position in the wall ($y \approx 1500$ nm). This suggests a more even mixture of the Néel and Bloch components in the wall.

As a first approach to avoid spatial dependence and allow us to compare simulations with manageable analytical expressions such as those from Ref. [36], an approximate value for the magnitude of the demagnetizing field transversal to the wall, assumed to be constant in its length, can be obtained from $\mu_0 H_d = \sqrt{(\mu_0 H_{d,x})^2 + (\mu_0 H_{d,z})^2}$, by retrieving from simulations the values of the components at properly selected locations in the y direction. Firstly, $\mu_0 H_{d,x} = 0.1$ T and $\mu_0 H_{d,z} = 0.05$ T were chosen, obtained from micromagnetic results at $y = 1500$ nm, i.e., halfway in the domain wall when no bias is applied (see blue curves in Fig. 6). This yields an approximate value for $\mu_0 H_d$ of 0.08 T, close to that of the fitting result shown in Fig. 4(a) ($\mu_0 H_d = 0.06$ T). If we choose the values at the edge of the vortex core, at the right edge of the blue shaded area in Fig. 6, $\mu_0 H_{d,x} = 0.07$ T and $\mu_0 H_{d,z} \approx 0$ T, the value of H_d is even closer. These observations suggest that effects such as mixed Bloch and Néel domain walls [39], should be considered for a more accurate quantitative description of these spin wave dynamics.

In summary, external biasing fields modify the local resonances in the wall region. In turn, a different local ferromagnetic resonance condition for the spin wave transmission in the wall is configured, as has been explored in this section. Considering the previously discussed points, the main reason behind a larger amplitude at positive biasing fields is suggested to be a better matching with the local ferromagnetic resonance in the Bloch wall for a given uniform biasing field.

Further analysis on the spin wave dynamics, other than the Winter's magnons, is not in the scope of the main body in this paper. However, in the Supplemental Material [40], we provide VNA-FMR measurements that suggest different spin wave dynamics depending on the initial relaxed state for the teardrop (SMV or DMV state). The different absorption footprints in the VNA-FMR plots for different bias [40] reveal that the SMV state is experimentally achievable in the teardrop shape, and also agree with the different hysteretic behavior of the teardrop shape, discussed in Sec. III.

V. FINAL DISCUSSIONS

In this section we discuss some of the main results previously shown, that make the teardrop patch an interesting structure for performing as a tunable, unidirectional spin wave emitter. Also, we further discuss the characterized spin wave modes in the patch, and how they relate to the required magnetic state for the teardrop to perform as such an emitter.

Spin wave emissions from sharp corners have been found in triangular shapes [12] in a B state (quasisaturated along one side of the triangle) and in the Y state (quasisaturated perpendicular to one side). The teardrop shape can be regarded as a combination of a triangular shape and a circular disk and so, the mentioned B or Y states can be partially obtained from a perpendicular or parallel biasing VNA-FMR scheme, respectively. Indeed, longer wavelength "edge" spin waves were observed in the teardrop shape in animations for a biasing parallel to the wall (see third movie in the Supplemental Movies [40]). In contrast to other geometries, while the vertex position is fixed, the single Bloch domain wall in the teardrop shape can be pinned at different positions along the curved edge, since it is a consequence of a single shifted vortex core. This provides more degrees of freedom when using the teardrop shape as a spin wave emitter and a potential edge spin wave interferometer, due to the high configurability of the two sources (vertex and nucleated Bloch domain wall near the curved edge).

Note that, for the perpendicular biasing scheme in the SMV state, these "edge modes" from the vertex were not found (see first and second animations in the Supplemental movies [40]). We believe that the single domain wall, while being stable and pinned at the sharp corner in the SMV state (and until vortex or domain wall annihilating fields are reached), inhibits the emission of the vertex spin waves that travel along the edges. The demagnetizing field at the teardrop vertex is different from that of the edges, which must inhibit the emission and consequent channeling of the edge spin wave for which a same local ferromagnetic resonance is required. Only at intermediate states between near saturation and the DMV state (in a quasi-B state), the top vertex emits spin waves.

After identifying all the relevant eigenmodes of the sample (see Supplemental Material [40]), we can confidently correlate the measured absorptions with spin wave modes in a variety of multidomain states of the teardrop shape, in turn identified from VSM measurements. To summarize, in the perpendicular pumping configuration one of the measured modes (mode I′) is enhanced and stable with the biasing field. Another mode, related to a domain resonance, coexists and grows transforming into a Kittel-like FMR mode. More importantly, we suggest that this can also be an indicator that the SMV state was previously formed.

The SMV state in a teardrop shape is the required configuration for the use of a confined vortex core as a tunable unidirectional emitter of confined spin waves, as shown in the conducted micromagnetic study in Sec. IV. We performed further analytical, micromagnetic, and experimental studies on the resonance conditions of the Winter's modes and other spin wave modes in the teardrop shape; these can be found in the Supplemental Material [40].

VI. SUMMARY

We have studied the magnetostatic response from a teardrop-shaped nanostructure in the multidomain and vortex state configurations. Micromagnetic results show its hysteretic behavior, confirmed by VSM measurements. VSM

measurements help to characterize the magnetic configurations allowed in the shape, as well as identify unidirectional Winter's magnons efficiently propagating in the shape for particular magnetic equilibrium states. Two different stable states, the SMV and the DMV can be set in the teardrop, being the former is a necessary state for Winter's magnons unidirectionality. Other spin wave dynamics have also been explored by means of micromagnetic simulations and the VNA-FMR technique for different measurement schemes, which allow us to identify different mode conversions from the two different stable states.

However, the main result of this work is not just the observation of the differences between VNA-FMR measurement schemes on the teardrop shape or even the different modes transformation between states, but to show that the SMV is achievable and stable (no biasing field to retain the magnetic configuration is required) in the nonsaturated regime. For a thick enough sample, features of some dominant spin wave modes in this state are potentially detectable in VNA-FMR absorption spectra.

Once the SMV state is obtained, the effects of external biasing fields on confined spin wave modes, varying magnitude, and orientation, have been explored by micromagnetic simulations, showing highly tunable properties. Results show that the SMV state in a teardrop-shaped patch, is ideal as a simple highly directional and reconfigurable spin wave emitter by exploiting modes confined to a single domain wall and emitted from a vortex core. We believe these results can help in further research, development, and improvement of spin wave emitters that do not require high biasing fields for operating in a wide range of excitation frequencies.

All data created during this research are openly available from the University of Exeter's institutional repository [45].

ACKNOWLEDGMENT

This work was supported by Engineering and Physical Sciences Research Council (EPSRC) and the Centre of Doctoral Training (CDT) Grant No. EP/L015331/1 in Metamaterials, University of Exeter.

[1] T. Shinjo, T. Okuno, R. Hassdorf, K. Shigeto, and T. Ono, Science **289**, 930 (2000).
[2] V. V. Kruglyak, S. O. Demokritov, and D. Grundler, J. Phys. D **43**, 264001 (2010).
[3] A. D. Karenowska, A. V. Chumak, A. A. Serga, and B. Hillebrands, Magnon spintronics, in *Handbook of Spintronics*, edited by Y. Xu, D. D. Awschalom, and J. Nitta (Springer Netherlands, Dordrecht, 2016), pp. 1505–1549.
[4] A. Hoffmann and S. D. Bader, Phys. Rev. Appl. **4**, 047001 (2015).
[5] C. S. Davies, V. D. Poimanov, and V. V. Kruglyak, Phys. Rev. B **96**, 094430 (2017).
[6] S. Wintz, V. Tiberkevich, M. Weigand, J. Raabe, J. Lindner, A. Erbe, A. Slavin, and J. Fassbender, Nat. Nanotechnol. **11**, 948 (2016).
[7] C. Behncke, C. Adolff, N. Lenzing, M. Hänze, B. Schulte, M. Weigand, and G. Meier, Commun. Phys. **1**, 50 (2018).
[8] G. Dieterle, J. Förster, H. Stoll, A. S. Semisalova, S. Finizio, A. Gangwar, M. Weigand, M. Noske, M. Fähnle, I. Bykova *et al.*, Phys. Rev. Lett. **122**, 117202 (2019).
[9] V. Sluka, T. Schneider, R. Gallardo, A. Kakay, M. Weigand, T. Warnatz, R. Mattheis, A. Roldán-Molina, P. Landeros, V. Tiberkevich *et al.*, Nat. Nanotechnol. **14**, 328 (2019).
[10] S. Mayr, L. Flajšman, S. Finizio, A. Hrabec, M. Weigand, J. Förster, H. Stoll, L. J. Heyderman, M. Urbánek, S. Wintz, and J. Raabe, Nano Lett. **21**, 1584 (2021).
[11] F. B. Mushenok, R. Dost, C. S. Davies, D. A. Allwood, B. J. Inkson, G. Hrkac, and V. V. Kruglyak, Appl. Phys. Lett. **111**, 042404 (2017).
[12] A. Lara, V. Metlushko, and F. G. Aliev, J. Appl. Phys. **114**, 213905 (2013).
[13] A. Lara, J. R. Moreno, K. Y. Guslienko, and F. G. Aliev, Sci. Rep. **7**, 5597 (2017).
[14] J. M. Winter, Phys. Rev. **124**, 452 (1961).
[15] X. S. Wang, H. W. Zhang, and X. R. Wang, Phys. Rev. Appl. **9**, 024029 (2018).
[16] N. J. Whitehead, S. A. R. Horsley, T. G. Philbin, A. N. Kuchko, and V. V. Kruglyak, Phys. Rev. B **96**, 064415 (2017).
[17] E. Albisetti, D. Petti, G. Sala, R. Silvani, S. Tacchi, S. Finizio, S. Wintz, A. Calo, X. Zheng, J. Raabe *et al.*, Commun. Phys. **1**, 56 (2018).
[18] K. Vogt, F. Y. Fradin, J. E. Pearson, T. Sebastian, S. D. Bader, B. Hillebrands, A. Hoffmann, and H. Schultheiss, Nat. Commun. **5**, 3727 (2014).
[19] K. Wagner, A. Kákay, K. Schultheiss, A. Henschke, T. Sebastian, and H. Schultheiss, Nat. Nanotechnol. **11**, 432 (2016).
[20] A. Yamaguchi, H. Hata, M. Goto, M. Kodama, Y. Kasatani, K. Sekiguchi, Y. Nozaki, T. Ohkochi, M. Kotsugi, and T. Kinoshita, Jpn. J. Appl. Phys. **55**, 023002 (2016).
[21] L.-J. Chang, J. Chen, D. Qu, L.-Z. Tsai, Y.-F. Liu, M.-Y. Kao, J.-Z. Liang, T.-S. Wu, T.-M. Chuang, H. Yu, and S.-F. Lee, Nano Lett. **20**, 3140 (2020).
[22] A. Vansteenkiste, J. Leliaert, M. Dvornik, M. Helsen, F. Garcia-Sanchez, and B. Van Waeyenberge, AIP Adv. **4**, 107133 (2014).
[23] J. Wang, X. Zhang, X. Lu, J. Zhang, Y. Yan, H. Ling, J. Wu, Y. Zhou, and Y. Xu, Appl. Phys. Lett. **111**, 072401 (2017).
[24] H. Nyquist, Trans. Am. Inst. Electr. Eng. **47**, 617 (1928).
[25] A. N. Broers, IBM J. Res. Dev. **32**, 502 (1988).
[26] S. O. Martinez-Chapa, A. Salazar, and M. J. Madou, Two-photon polymerization as a component of desktop integrated manufacturing platforms, in *Three-Dimensional Microfabrication Using Two-Photon Polymerization: Fundamentals, Technology, and Applications*, edited by T. Baldacchini (Elsevier, Dordrecht, 2016), pp. 374–416.
[27] F. Abreu Araujo, A. D. Belanovsky, P. N. Skirdkov, K. A. Zvezdin, A. K. Zvezdin, N. Locatelli, R. Lebrun, J. Grollier, V. Cros, G. de Loubens, and O. Klein, Phys. Rev. B **92**, 045419 (2015).
[28] Y. Li, X. de Milly, F. Abreu Araujo, O. Klein, V. Cros, J. Grollier, and G. de Loubens, Phys. Rev. Lett. **118**, 247202 (2017).

[29] I. Neudecker, K. Perzlmaier, F. Hoffmann, G. Woltersdorf, M. Buess, D. Weiss, and C. H. Back, Phys. Rev. B **73**, 134426 (2006).
[30] F. G. Aliev, J. F. Sierra, A. A. Awad, G. N. Kakazei, D.-S. Han, S.-K. Kim, V. Metlushko, B. Ilic, and K. Y. Guslienko, Phys. Rev. B **79**, 174433 (2009).
[31] C. A. F. Vaz, M. Kläui, L. J. Heyderman, C. David, F. Nolting, and J. A. C. Bland, Phys. Rev. B **72**, 224426 (2005).
[32] F. G. Aliev, A. A. Awad, D. Dieleman, A. Lara, V. Metlushko, and K. Y. Guslienko, Phys. Rev. B **84**, 144406 (2011).
[33] P. Vavassori, N. Zaluzec, V. Metlushko, V. Novosad, B. Ilic, and M. Grimsditch, Phys. Rev. B **69**, 214404 (2004).
[34] S. Yakata, T. Tanaka, K. Kiseki, K. Matsuyama, and T. Kimura, Sci. Rep. **3**, 3567 (2013).
[35] M. Vaňatka, M. Urbánek, R. Jíra, L. Flajšman, M. Dhankhar, M.-Y. Im, J. Michalička, V. Uhlíř, and T. Šikola, AIP Adv. **7**, 105103 (2017).
[36] F. Garcia-Sanchez, P. Borys, R. Soucaille, J.-P. Adam, R. L. Stamps, and J.-V. Kim, Phys. Rev. Lett. **114**, 247206 (2015).
[37] E. J. Torok, A. L. Olson, and H. N. Oredson, J. Appl. Phys. **36**, 1394 (1965).
[38] A. L. Olson, H. N. Oredson, E. J. Torok, and R. A. Spurrier, J. Appl. Phys. **38**, 1349 (1967).
[39] D. Osuna Ruiz, A. P. Hibbins, and F. Y. Ogrin, Phys. Rev. B **102**, 224431 (2020).
[40] See Supplemental Material at http://link.aps.org/supplemental/10.1103/PhysRevB.104.094427 for more details in the corresponding section, which includes Refs. [12,16,30,35,36,43,44].
[41] X.-G. Wang, G.-H. Guo, G.-F. Zhang, Y.-Z. Nie, and Q.-L. Xia, J. Appl. Phys. **113**, 213904 (2013).
[42] L.-J. Chang, Y.-F. Liu, M.-Y. Kao, L.-Z. Tsai, J.-Z. Liang, and S.-F. Lee, Sci. Rep. **8**, 3910 (2018).
[43] D. Osuna Ruiz, E. B. Parra, N. Bukin, M. Heath, A. Lara, F. G. Aliev, A. P. Hibbins, and F. Y. Ogrin, Phys. Rev. B **100**, 214437 (2019).
[44] A. Savitzky and M. J. E. Golay, Anal. Chem. **36**, 1627 (1964).
[45] https://ore.exeter.ac.uk/repository/.